Implementation of a 9-point stencil in SOLPS-ITER and implications for Alcator C-Mod divertor plasma simulations

Wouter Dekeyser[*],[a], Xavier Bonnin[b], Steven W. Lisgo[b], Richard A. Pitts[b], Brian LaBombard[c]

[a] KU Leuven, Department of Mechanical Engineering, Celestijnenlaan 300, Leuven 3001, Belgium
[b] ITER Organization, Route de Vinon-sur-Verdon, CS 90 046, St Paul Lez Durance 13067, France
[c] MIT Plasma Science and Fusion Center, Cambridge, MA 02139, USA

ARTICLE INFO

ABSTRACT

The SOLPS-ITER code suite is used worldwide for plasma edge modeling, the interpretation of experiments, as well as for the design of the ITER divertor. The numerical scheme of the plasma solver of the code, B2.5, is based on the assumption of perfectly orthogonal grids in the poloidal plane, aligned with the magnetic field, while in practice grids are often strongly distorted to match divertor target shapes. Neglecting these grid distortion leads to qualitatively and quantitatively incorrect results for fluid neutral simulations, and may affect results in cold (detached) divertors even when using kinetic neutral simulations. In this contribution, we present the first results of a newly implemented 9-point stencil in B2.5 to properly handle misaligned grids. The new scheme is then applied to fluid neutral simulations of a well-diagnosed and previously modeled Alcator C-Mod discharge. Results are compared with the original 5-point scheme neglecting grid distortion effects, as well as with simulations including a full kinetic neutral model. We conclude that the 9-point stencil is essential to correctly model the transport of fluid neutrals on distorted grids, and to capture the effects of divertor closure on the fluid neutral behavior.

1. Introduction

The SOLPS code suite has been used as the workhorse for the design of the ITER divertor [1]. The latest version of the code, SOLPS-ITER [2,3], is based on an up-to-date version of EIRENE and includes the advanced fluid drifts model from SOLPS5.2.

One of the ongoing developments of the code aims at enabling the use of grids extending up to the vessel wall. In this contribution, we report on a part of this effort that involves improving the discretization of the underlying plasma equations. Presently, the plasma solver in the code, B2.5, assumes perfectly orthogonal grids in the poloidal plane, aligned with the magnetic field. However, such grids are not compatible with the strongly shaped divertor targets in most current machines, and as foreseen on ITER. Therefore, in practice the grids are only aligned with the magnetic surfaces, but radial lines may be far from orthogonal to the field. While several other plasma edge codes correctly discretize the plasma equations on misaligned grids [4–7], these distortion effects have been neglected in B2.5 thus far. Note however that EIRENE, which models kinetic neutral transport in SOLPS(-ITER), does correctly account for grid nonorthogonality.

Correctly accounting for grid distortion in the simulations is especially important for fluid neutral models, because neutral transport is isotropic. Neglecting grid distortion for fluid neutrals leads to both qualitatively and quantitatively incorrect divertor solutions [6]. The situation is somewhat less problematic for plasma transport, because the transport is dominated by fast parallel convection and conduction. Grids are still aligned in the parallel (poloidal) direction, hence this component of transport is correctly discretized. However, in the cold divertor conditions found in high-recycling and detached regimes, as expected in ITER, this argument no longer holds. Radial transport could become comparable in magnitude to parallel transport, so its proper discretization becomes important, especially since it is exactly in the divertor that grids are most strongly misaligned.

In this paper, we discuss the implementation of a 9-point stencil in B2.5 to account for grid distortion. Section 2 describes the implementation of the 9-point stencil based on a generic, anisotropic convection-diffusion equation. The new code is then applied to Alcator C-Mod divertor simulations in Section 3. Finally, conclusions and perspectives are summarized in Section 4.

---

[*] Corresponding author.
  E-mail address: wouter.dekeyser@kuleuven.be (W. Dekeyser).

2. Discretization of the governing equations on misaligned grids

The plasma transport solver in SOLPS-ITER, B2.5, solves a set of continuity and parallel momentum equations for the ions and (atomic) neutral species in the plasma, as well as ion and electron internal energy equations. The equation for the plasma potential is derived from the condition that the divergence of the currents must be zero. For the parallel direction, classical transport according to Braginskii is assumed, while anomalous radial transport is approximated by a typical diffusive ansatz, with anomalous diffusivities and conductivities determined to match experimentally measured profiles. These equations are solved in the 2D poloidal plane, assuming symmetry in the third, toroidal direction.

In general, each of the governing equations can be regarded as a nonlinear, anisotropic convection–diffusion equation of the form

$$\frac{\partial \phi}{\partial t} + \nabla \cdot \mathbf{\Gamma} = S, \tag{1}$$

where ϕ is a transported quantity (density, parallel velocity, temperature or potential), $\mathbf{\Gamma}$ the corresponding flux, and S a source term in the equation. The flux of a particular quantity can in general be decomposed into a convective and a diffusive piece as

$$\mathbf{\Gamma} = \mathbf{C}\phi - D\nabla\phi. \tag{2}$$

The anisotropy in the equations is most naturally expressed in a curvilinear poloidal-radial coordinate system $\{\theta, r\}$, with respective unit vectors $\mathbf{b}$ and $\mathbf{e}_r$. The coefficient $\mathbf{C} = C_\theta \mathbf{e}_\theta + C_r \mathbf{e}_r$ in Eq. (2) is a vector describing the convective flux of ϕ, with components defined in the poloidal and radial directions, and $D = [D_{\theta\theta}D_{\theta r}, D_{r\theta}D_{rr}]$ a diffusive tensor. The cross-diffusivities $D_{\theta r}$ and $D_{r\theta}$ are included here because they are representative for the treatment of drift flows, see below. In B2.5, the balance Eq. (1) are discretized using a Finite-Volume technique, which requires the evaluation of the fluxes (2) across cell faces:

$$
\begin{aligned}
\mathbf{\Gamma} \cdot \mathbf{S} &= \Gamma_\theta S_\theta + \Gamma_r S_r, \\
&= (C_\theta \phi - D_{\theta\theta}\nabla_\theta\phi - D_{\theta r}\nabla_r\phi)S_\theta + (C_r\phi - D_{r\theta}\nabla_\theta\phi - D_{rr}\nabla_r\phi)S_r.
\end{aligned} \tag{3}
$$

Here, $\mathbf{S} = S_\theta \mathbf{e}_\theta + S_r \mathbf{e}_r$ is the surface vector of a face, expanded in its poloidal and radial components.

B2.5 was originally developed with orthogonal, field-aligned grids in mind. The equations are discretized on a topologically rectangular, (block-)structured grid, which can be described in the curvilinear grid coordinate system $\{x, y\}$. In this coordinate system, it is assumed that the first coordinate direction, x, is aligned with the poloidal direction θ, while the second coordinate direction, y, is aligned with the radial direction r. A schematic representation of such a grid, indicating the coordinate systems, is given in Fig. 1. In the case of such orthogonal grids, both the $\{x, y\}$ and $\{\theta, r\}$ coordinate systems are orthogonal, and they coincide. In the figure, 'poloidal' faces o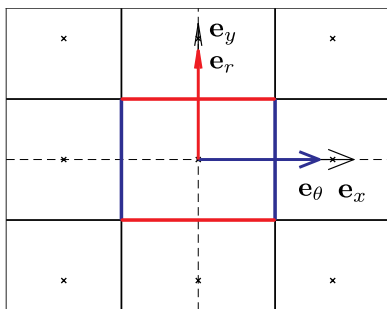r 'x' faces of the central cell are indicated in blue, and 'radial' faces ('y' faces) in red. It is trivially seen that the poloidal and radial gradients required to evaluate the fluxes in Eq. (3) can be computed by taking derivatives along the grid directions,

$$\nabla_\theta\phi = \nabla_x\phi, \tag{4}$$

$$\nabla_r\phi = \nabla_y\phi. \tag{5}$$

Moreover, since surfaces are either aligned with or orthogonal to the field, Eq. (3) shows that there is only a poloidal flux across 'x' faces (faces with $S_r = 0$), and only a radial flux across 'y' faces (faces with $S_\theta = 0$). If drifts are neglected ($D_{\theta r} = D_{r\theta} = 0$), evaluating Eq. (3) across the four faces of a cell and taking the divergence leads to a so-called '5-point stencil' equation, in which the equation for the value of $\phi_{i,j}$ in cell $\{i, j\}$ depends only on the value of ϕ in the cell itself and in its neighbors $\{i - 1, j\}$, $\{i + 1, j\}$, $\{i, j - 1\}$ and $\{i, j + 1\}$.

In practical configurations, however, the vessel structures are almost never perfectly orthogonal to the poloidal projection of the field lines. An example is shown in Fig. 3, where a strongly distorted plasma grid (blue) is shown for the old Alcator C-Mod divertor. The y grid lines are distorted to match the divertor target surface, while x grid lines are kept aligned with the poloidal direction for a correct discretization of the (fast) parallel flows. The two curvilinear coordinate systems no longer coincide: the physical poloidal-radial system $\{\theta, r\}$ remains fully orthogonal by definition, while the grid system $\{x, y\}$ becomes non-orthogonal. The latter system is easily related to the physical system by a (local) angle γ, see Fig. 2, which shows a zoom of the grid in Fig. 3 near the inner target.

When inspecting Eq. (3), there are two important effects of such misaligned grids. First of all, while the poloidal gradients can still be computed by taking the derivatives along the x-direction, computation of radial gradients becomes more involved. The relation between the components of the gradient in both coordinate systems can be obtained most easily by expanding the gradient in the orthogonal poloidal–radial system, $\nabla\phi = \nabla_\theta\phi\,\mathbf{e}_\theta + \nabla_r\phi\,\mathbf{e}_r$, and applying the definition of the gradient, $\nabla_d\phi = \nabla\phi\cdot\mathbf{d}$ for an arbitrary direction $\mathbf{d}$, to the unit vectors $\mathbf{e}_x$ and $\mathbf{e}_y$:

$$
\begin{aligned}
\nabla_x\phi &= \nabla\phi\cdot\mathbf{e}_x &=& \quad \nabla_\theta\phi\,\mathbf{e}_\theta\cdot\mathbf{e}_x + \nabla_r\phi\,\mathbf{e}_r\cdot\mathbf{e}_x, \\
\nabla_y\phi &= \nabla\phi\cdot\mathbf{e}_y &=& \quad \nabla_\theta\phi\,\mathbf{e}_\theta\cdot\mathbf{e}_y + \nabla_r\phi\,\mathbf{e}_r\cdot\mathbf{e}_y.
\end{aligned}
$$

Noting that $\mathbf{e}_\theta\cdot\mathbf{e}_x = 1$, $\mathbf{e}_r\cdot\mathbf{e}_x = 0$, $\mathbf{e}_\theta\cdot\mathbf{e}_y = \sin\gamma$ and $\mathbf{e}_r\cdot\mathbf{e}_y = \cos\gamma$, this system can then be inverted to obtain the poloidal and radial components of the gradient as a function of the x and y components available on the grid:

$$\nabla_\theta\phi = \nabla_x\phi, \tag{6}$$

$$\nabla_r\phi = \frac{1}{\cos\gamma}\nabla_y\phi - \tan\gamma\,\nabla_x\phi. \tag{7}$$

Hence, computing the components of the gradient in the radial

Fig. 1. Definition of coordinate systems for aligned meshes. Grid system and poloidal– radial system coincide.
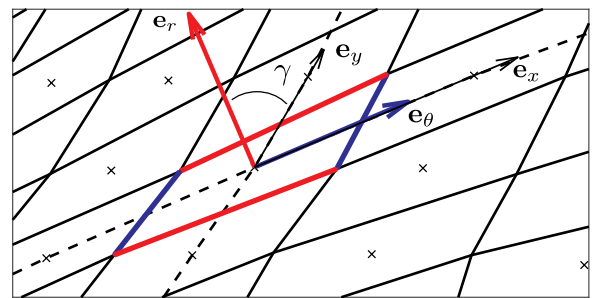

Fig. 2. Definition of coordinate systems for misaligned meshes. Non-orthogonal grid system, but orthogonal poloidal–radial system.
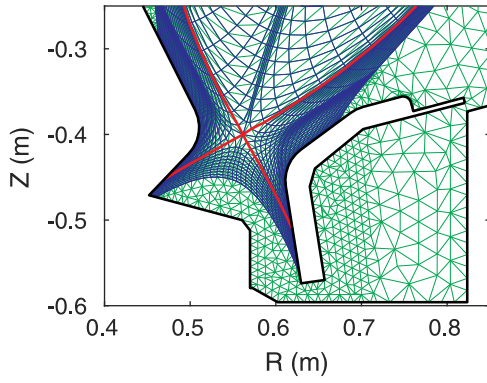
Fig. 3. An example of a strongly distorted mesh due to inclined divertor targets (Alcator C-Mod).

direction not only requires taking differences along the y direction, but also along the x direction. Computing the radial gradients now involves also the values of ϕ defined at cell vertices, leading in general to a so-called '9-point stencil', where the balance equation for the cells depends on the cell itself and its 8 surrounding neighbors. Note that the expressions for gradients on orthogonal grids, Eqs. (4) and (5), are just special instances of Eqs. (6) and (7) corresponding to $\gamma = 0$. The second important effect is that there are now both poloidal *and* radial flows across x-surfaces (blue faces in Fig. 2), and not only poloidal flows as is the case on purely orthogonal grids. This is particularly important for fluid neutral simulations, as the radial flow component may completely dominate the poloidal one, as will be illustrated below.

Finally, we comment briefly on the treatment of drifts in the 9-point stencil code. In the balance equations, only the drift flows perpendicular to a face will lead to transport across a face. Since all drift flows have a general structure of $\nabla\phi \times \mathbf{B}$, they eventually appear as cross-diffusion terms in Eq. (3), with $D_{\theta r} = -D_{r\theta} = D_{\mathrm{d}}$. The net drift flow $\mathbf{\Gamma}_{\mathrm{d}}$ across a face is thus of the form

$$\mathbf{\Gamma}_{\mathrm{d}} \cdot \mathbf{S} = -D_{\mathrm{d}}(\nabla_r \phi S_\theta - \nabla_\theta \phi S_r), \tag{8}$$

where the term between parentheses is the product of the face area S with the component of the gradient *parallel* to the face, as expected from the physics. Thus, net drift flow across the face only depends on gradients along the face, while the decomposition of the drift in its poloidal and radial components (as needed for example for the collisions with neutrals) requires again the correct computation of both (poloidal and) radial gradients on the misaligned grids.

The corrections to the discretization of the basic equations described above have now been implemented into B2.5, for the reference model including drifts from Ref. [8]. The implementation ensures full backwards compatibility for existing cases.

3. Application to Alcator C-Mod simulations

In this section, we apply the new 9-point stencil code to Alcator C-Mod divertor plasma simulations, for discharge 990429019. The discharge, which has detached (cold) inner divertor and outer divertor in high-recycling conditions, has already been subject of intense numerical studies using the SOLPS-ITER code [9,10]. Moreover, C-Mod has an ITER-relevant magnetic field, and the (old) C-Mod divertor has strong, ITER-like, shaping, and thus provides an ideal testbed for the new code. In the next subsection, we briefly summarize the experimental discharge and the numerical setup. Then we zoom in on the simulation results, first for simulations with a fluid neutral model without drifts, followed by some short comments about complete simulations with kinetic neutral model (using EIRENE [11]) and drifts.

3.1. Experiment and numerical setup

As a continuation of our previous studies, we use the deuterium, ohmic discharge number 990429019 at 950 ms. The plasma current for this discharge is $I_{\mathrm{p}} = 0.8$ MA, with toroidal field $B_{\mathrm{T}} = 5.4$ T, and a line average density of $\bar{n}_{\mathrm{e}} = 1.46 \cdot 10^{20}$ m^{-3}, a medium-density discharge on C-Mod. The magnetic geometry is single-null, with lower X-point, and the ion $B \times \nabla B$ drift direction pointing down. The ohmic power obtained from an EFIT-reconstruction is $P_{\mathrm{OH}} \sim 1$ MW, and radiated power in the core measured with a diode detector is estimated at $P_{\mathrm{rad}} \sim 500$ kW. Simulation results will be compared to outer midplane profiles of electron density and temperature obtained with a Horizontal Scanning Probe (HSP), and to data from Langmuir Probes (LP) embedded in the divertor targets. As is typical for C-Mod discharges, the inner target LP data shows clear detachment near the strike point, while the outer target is in a high recycling state.

In previous work, we have already modeled this discharge extensively, first using fluid neutral models without drifts in Ref. [9], and eventually using a complete kinetic neutral model (EIRENE) and including plasma drifts in Ref. [10]. For details of the numerical setup and input parameters, we refer to those publications. Here we only summarize some of the most important elements. The simulations use standard sheath boundary conditions at the divertor targets, while core boundary conditions are imposed based on the experimental density and power. Radial profiles of anomalous transport coefficients are determined to match the profiles of electron density and temperature measured by the HSP at the outer midplane. These transport coefficient profiles are kept constant in the poloidal direction.

In the present paper, the focus is entirely on the effect of the 9-point stencil on the resulting simulations. Therefore, we re-performed a few representative simulations from our earlier study, using identical input parameters, but adopting the improved treatment of misaligned grids. The grid used for these simulations has 80 poloidal and 30 radial grid cells. Fig. 3 shows a zoom of this grid in the divertor area. The blue lines represent the grid used for the plasma, showing the strong distortion of the radial gridlines required to match the shaped, vertical targets of the old C-Mod divertor. The green triangles represent the grid required for kinetic neutral simulations (not used in case of fluid neutral simulations).

3.2. Fluid neutral simulations

In this section we assess the impact of the 9-point stencil on simulations using a fluid neutral model, without drifts. We use the reference case described in Ref. [9], with and without the new 9-point stencil. In a fluid neutral model, the neutrals are modeled by a continuity and parallel momentum equation, and are assumed to have the same temperature as the ions. In the radial and diamagnetic directions, neutral transport is modeled using a pressure diffusion assumption. The resulting neutral particle flux $\mathbf{\Gamma}_{\mathrm{n}}$ is

$$\mathbf{\Gamma}_{\mathrm{n}} = n_{\mathrm{n}} u_{\parallel,\mathrm{n}} \mathbf{b} - D^{\mathrm{p}} \nabla p_{\mathrm{n}}, \tag{9}$$

with n_{n} the neutral density, $u_{\parallel,\mathrm{n}}$ the neutral parallel velocity, and $p_{\mathrm{n}} = n_{\mathrm{n}} T_{\mathrm{i}}$ the neutral pressure. T_{i} is the common ion-neutral temperature, and $\mathbf{b}$ the unit vector in the direction of the magnetic field. The neutral parallel velocity is obtained by solving a parallel momentum equation for the neutral species. It is to be noted that in contrast to the equations for ionized species (ions/electrons), the pressure diffusion coefficient of the neutrals, D^{p}, is isotropic. Especially for these fluid neutral simulations we expect the impact of the 9-point stencil to be large, because an incorrect treatment of grid distortion with a 5-point treatment —— which correctly models poloidal transport, but incorrectly captures the radial gradients —— artificially introduces anisotropy in the fluid neutral model.
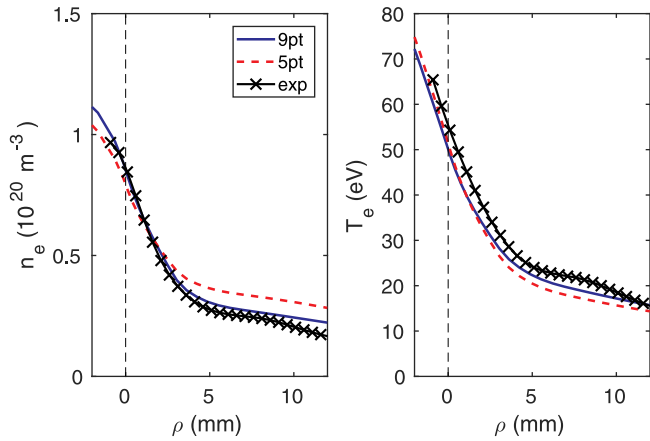
Fig. 4. Electron density and temperature at the outer midplane, as computed with 9-point (solid lines) and 5-point (dashed lines) stencil code versions, compared to experiment.
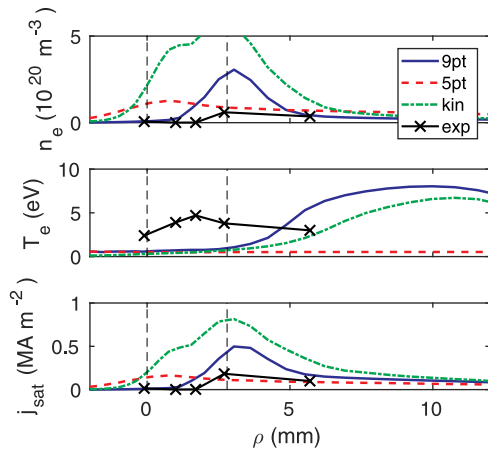

Fig. 5. Profiles of electron density, electron temperature and saturation current at the inner target.

First, we look at the profiles of electron density and temperature at the outer midplane, Fig. 4. They are only slightly impacted by the change in scheme. Since the transport coefficients have been tuned to match these profiles, the general agreement is good. Next we compare the simulated profiles of ion saturation current j_{sat}, electron temperature T_e, and electron density n_e at the inner target but mapped to the midplane, Fig. 5. It is immediately obvious that the results of 5-point and 9-point simulations are both qualitatively and quantitatively

different here. The profiles of n_e and j_{sat} obtained with the 5-point stencil tend to peak close to the separatrix strike point ($\rho = 0$). In contrast, the profiles obtained with the 9-point stencil peak around the nose of the inner divertor, indicated with the dashed vertical line at $\rho \sim 3$ mm. While the temperature obtained with the 5-point scheme is low and nearly constant along the entire target, it clearly rises again above the nose in the 9-point stencil case. We also observe that in the 5-point case, this target is quite uniformly detached in this simulation (so also the remaining peaks near the strike points are quite low), while in the 9-point case we have a clear, strong suppression of j_{sat} below the nose, but a (small) rise of j_{sat} above the nose. Qualitatively, the 9-point stencil results are in much better agreement with experiment.

To further interpret these results, we also compare qualitatively to the results of a fully coupled B2.5-EIRENE simulation, i.e. with kinetic neutrals. The profiles obtained with the kinetic neutral simulation are also added in Fig. 5. To be able to compare with this kinetic simulation, care has to be taken with the geometry. Indeed, in Alcator C-Mod, a number of pathways are available for neutral leakage from the divertor to the main chamber, including an important leakage through the divertor plenum behind the outer target [12,13]. In earlier work [10], we pointed out that including these leakage paths is important to improve the match with experiment. However, in the present paper we want to achieve a qualitative comparison with a fluid neutral model. Since the fluid neutrals are confined to the plasma grid and hence cannot escape through the plenum, we compare to the simulation with closed plenum geometry described in Ref. [10]. We remark that the kinetic simulation contains a complete physics description, including molecules and neutral-neutral collision, so a direct quantitative comparison is out of scope here. However, given that the C-Mod discharge under consideration has a high density divertor, we may expect that a fluid neutral model should be able to capture some of the basic physics of neutral compression in the divertor. While the quantitative results obtained with the full kinetic model differ quite substantially from the fluid neutral results, it is immediately obvious from Fig. 5 that qualitatively the behavior of 9-point and full kinetic simulations are the same. Similar qualitative observations hold for the outer target as well. We note, however, that symmetric inner-outer target solutions are typically found in simulations without drifts, see among other Ref. [10] for C-Mod simulations with drifts. Drifts are not included in our fluid neutral simulations, and hence we do not focus on the outer target here.

To investigate where the original 5-point scheme is failing, we analyze the spatial distribution of the neutrals in the divertor and their flow patterns. Fig. 6 shows the neutral density in the divertor, as obtained with the 9-point and 5-point stencil codes. For comparison, also the atom density obtained with the kinetic simulation is added here. Again we observe an essential difference between the 9-point and 5-point solutions. While in the 9-point solution the neutrals are strongly compressed below the divertor throat due to the tight baffling, the fluid neutrals in the 5-point stencil simulation seem to spread out along the
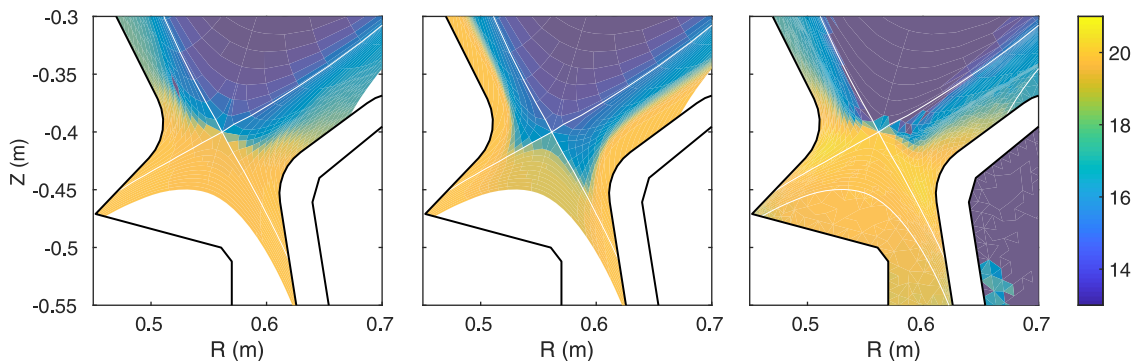

Fig. 6. Neutral density (atoms) in the divertor ($\log_{10} n_e$ [m^{-3}]), for case with 9-point stencil (left), 5-point stencil (middle), and kinetic neutrals (right).
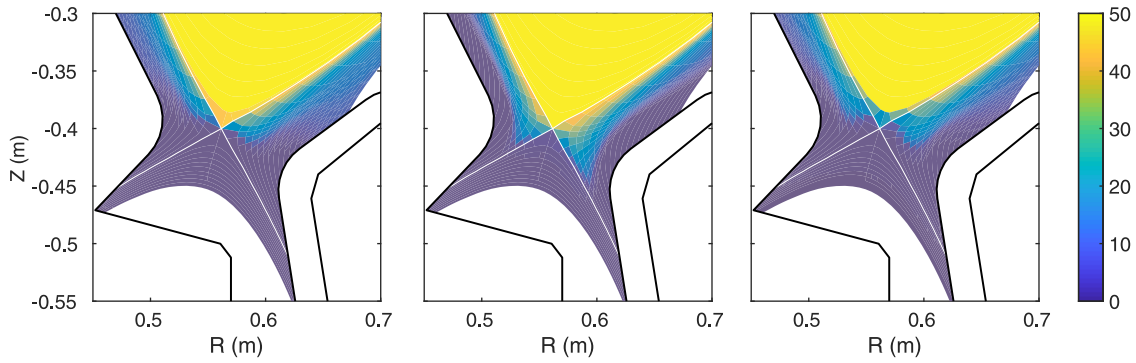
Fig. 7. Electron temperature in the divertor (eV), for case with 9-point stencil (left), 5-point stencil (middle), and kinetic neutrals (right).

entire surface of the targets towards the main chamber. This difference in neutral behavior is then reflected in the spatial profiles of the electron temperature, Fig. 7. High neutral density regions in the divertor correspond to cold temperatures, with an artificially low temperature all along the targets in the 5-point stencil case. While it is not obvious from the scale in the figures, the divertor in the 9-point case is substantially colder than in the 5-point case, which is in turn reflected in the strong detachment below the nose already observed in Fig. 5. By comparing qualitatively with a full kinetic simulation, we see that the 9-point case is qualitatively nearly identical to the full kinetic result.

Finally, to understand the artificial spreading of the neutrals along the targets in the 5-point stencil solution, we look at the streamlines of the fluid neutrals, Fig. 8. In that figure, the streamlines of fluid neutrals originating at the inner target are red, and of those originating at the outer target are green. The background coloring and contours indicate the neutral pressure. In the left figure, the streamlines of the 9-point stencil solution are shown. As expected from Eq. (9), the streamlines are everywhere nearly perpendicular to the contours of constant neutral pressure, since the neutral transport is dominated by pressure diffusion. The middle figure shows the streamlines and neutral pressure for the 5-point solution. In this case, there is a strong neutral cushion right in front of each target, but interestingly, the streamlines simulated by the code are not at all perpendicular to the contours of constant pressure. Rather, due to the neglect of the second term in Eq. (7), only the gradient of the neutral pressure *along* the target (the local *y*-direction) is felt by the numerical scheme, which now artificially pushes the neutrals nearly tangentially up along the targets instead of down the pressure gradient of the neutral cushion. The right graph in Fig. 8 computes the corrected streamlines using the full 9-point stencil, but on the background obtained with the 5-point stencil solution. These are now again nearly

perpendicular to the pressure contours. These modified streamlines strongly impact the neutral transport, and would push the solution away from the artificial equilibrium obtained with the 5-point stencil, to eventually reach the 9-point solution.

From these observations, we conclude that a full 9-point stencil treatment of the fluid neutrals is absolutely essential to correctly model their transport. The original 5-point stencil leads to qualitatively and quantitatively incorrect results, and cannot correctly capture the effect of target shaping on neutral transport and compression.

3.3. Kinetic neutral simulations

The new 9-point stencil scheme has also been applied to a number of C-Mod simulations from Ref. [10], including a complete kinetic neutral model and plasma drifts. In the interest of space, we do not show detailed results but only summarize some observations. The kinetic neutral model in EIRENE does not suffer from the 5-point approximations in B2.5, hence in these simulations only the plasma transport is impacted by the improved 9-point scheme. Since plasma transport is in general strongly anisotropic and dominated by the parallel (poloidal) flow component, it is much less sensitive to the approximations made by the 5-point stencil in the code. Indeed, the parallel (poloidal) flows are still properly discretized on the misaligned grids when using the original 5-point stencil. In our C-Mod simulations, we observe no significant changes to the target profiles near the separatrix strike points, but some increases in electron temperature and corresponding decreases in density towards the baffles are observed, similar to the results of the 9-point stencil simulation with fluid neutrals presented in Fig. 5. The spatial distributions of electron temperature and density in the divertor are also impacted, with changes of up to a factor two in both
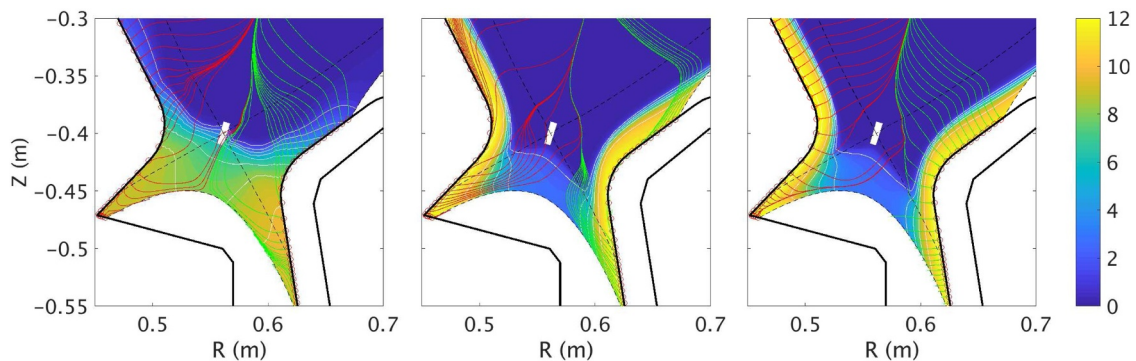

Fig. 8. Streamlines of the fluid neutrals, for case with 9-point stencil (left), 5-point stencil (middle), and flow calculated using the 9-point stencil on the background obtained with the 5-point stencil (right). Coloring: neutral pressure (Pa).

density and temperature, but again mainly towards the far Scrape-Off Layer (SOL) regions of the targets and far into the Private Flux areas. It remains to be investigated whether or not such changes could eventually impact impurity transport or far SOL flows.

4. Conclusion

In this paper, we have presented a 9-point stencil scheme for the correct discretization of the B2.5 transport equations on grids misaligned with the magnetic field. The new scheme has been applied to fluid neutral simulations of the Alcator C-Mod divertor plasma, and the results have been compared qualitatively to kinetic neutral simulations using EIRENE. We conclude that the 9-point stencil is essential to correctly model the transport of fluid neutrals on distorted grids. The original 5-point scheme cannot properly capture the impact of divertor shaping on fluid neutral simulations, leading to qualitatively and quantitatively incorrect results. For coupled B2.5-EIRENE simulations the impact of the new scheme is less pronounced, since plasma transport is dominated by fast parallel (poloidal) flows which are still correctly discretized by the original 5-point stencil scheme of the code.

The improved discretization opens up the way towards further code speed-up by using advanced fluid neutral [14,15] and hybrid fluid-kinetic [16,17] neutral models. These models have been shown to be very accurate compared to kinetic simulations in high recycling and detached regimes, at much reduced computational cost. Also in these models, a correct discretization of the fluid neutral solution will prove essential. The work is also an important first step towards the development of extended grids capabilities into B2.5, which will enable the simulation of the plasma all the way up to the main chamber wall.

References

[1] A.S. Kukushkin, H.D. Pacher, V. Kotov, et al., Fusion Eng. Des. 86 (2011) 2865–2873.
[2] S. Wiesen, D. Reiter, V. Kotov, et al., J. Nucl. Mater. 463 (2015) 480–484.
[3] X. Bonnin, W. Dekeyser, R.A. Pitts, et al., Plasma Fusion Res. 11 (2016) 1403102.
[4] R. Simonini, G. Corrigan, G. Radford, et al., Contrib. Plasma Phys. 34 (1994) 368–373.
[5] M.E. Rensink, D.A. Knoll, G. D. Porter, et al., IAEA technical committee meeting on advances in computer modeling of fusion plasmas, (1996). Los Angeles, CA, USA, Oct. 2–4
[6] W. Dekeyser, D. Reiter, M. Baelmans, Proc. Appl. Math. Mech. 14 (2014) 1017–1022.
[7] J. Leddy, B. Dudson, M. Romanelli, et al., Comput. Phys. Commun. 212 (2017) 59–68.
[8] V. Rozhansky, E. Kaveeva, P. Molchanov, et al., Nucl. Fusion 49 (2009) 025007.
[9] W. Dekeyser, X. Bonnin, S.W. Lisgo, et al., Plasma Fusion Res. 11 (2016) 1403103.
[10] W. Dekeyser, X. Bonnin, S.W. Lisgo, et al., Nuclear Mater. Energy 12 (2017) 899–907.
[11] D. Reiter, M. Baelmans, P. Boerner, Fusion Sci. Tech. 47 (2005) 172–186.
[12] C.S. Pitcher, C.J. Boswell, J.A. Goetz, et al., Phys. Plasmas 7 (2000) 1894–1903.
[13] C.S. Pitcher, C.J. Boswell, T. Chung, et al., J. Nucl. Mater. 290–293 (2001) 812–819.
[14] N. Horsten, W. Dekeyser, G. Samaey, et al., Nuclear Mater. Energy 12 (2017) 869–875.
[15] M. Blommaert, W. Dekeyser, N. Horsten, et al., Contrib. Plasma Phys. 58 (2018) 718–724.
[16] N. Horsten, et al., These proceedings.
[17] M. Blommaert, et al., These proceedings.